Spatially correlated incommensurate lattice modulations in an atomically thin high-temperature $Bi_{2.1}Sr_{1.9}CaCu_{2.0}O_{8+y}$ superconductor

Nicola Poccia [1,2] Shu Yang Frank Zhao,[2] Hyobin Yoo,[2] Xiaojing Huang,[3] Hanfei Yan,[3] Yong S. Chu,[3] Ruidan Zhong,[4]
Genda Gu,[4] Claudio Mazzoli,[3] Kenji Watanabe [5] Takashi Taniguchi,[6] Gaetano Campi,[7]
Valerii M. Vinokur [8,9] and Philip Kim[2,*]

[1]*Institute for Metallic Materials, IFW Dresden, 01069 Dresden, Germany*
[2]*Department of Physics, Harvard University, Cambridge, Massachusetts 02138, USA*
[3]*National Synchrotron Light Source II, Brookhaven National Laboratory, Upton, New York 11973-5000, USA*
[4]*Department of Condensed Matter Physics and Materials Science, Brookhaven National Laboratory, Upton, New York 11973-5000, USA*
[5]*Research Center for Functional Materials, National Institute for Materials Science, 1-1 Namiki, Tsukuba 305-0044, Japan*
[6]*International Center for Materials Nanoarchitectonics, National Institute for Materials Science, 1-1 Namiki, Tsukuba 305-0044, Japan*
[7]*Institute of Crystallography, CNR, via Salaria Km 29.300, Monterotondo Roma 00015, Italy*
[8]*Materials Science Division, Argonne National Laboratory, 9700 S. Cass Avenue, Argonne, Illinois 60637, USA*
[9]*Consortium for Advanced Science and Engineering (CASE), University of Chicago, 5801 S. Ellis Avenue, Chicago, Illinois 60637, USA*

We report high spatial resolution, below 100 nm, scanning nano x-ray diffraction (SnXRD) imaging of incommensurate lattice modulations (ILM) in $Bi_{2.1}Sr_{1.9}CaCu_{2.0}O_{8+y}$ van der Waals heterostructures of thicknesses down to two unit cells. We reveal the distinct long-range and short-range ILMs in a bulk sample and at the surface. We find that the size and mutual orientation of the puddlelike domains of the ILM are determined by the dimensionality of the system. In the two-unit-cell sample, the wave vectors of the long- and short-range orders become anticorrelated, and the emergent spatial patterns have a directional gradient. These emergent patterns imply static mesoscopic lattice modulation. Our findings open a route for local strain engineering to modulate properties of two-dimensional high-temperature superconductors.

I. INTRODUCTION

High-temperature superconducting cuprate perovskites are composed of CuO_2 layers intercalated between charge reservoir layers. The differences between these two structural units give rise to intriguing and unconventional crystallographic patterns up to the mesoscale which can control superconducting properties [1–9]. Although the c-axis period changes from one cuprate system to another due to different staging of dopants, incommensurate modulations along the b axis are common to optimally doped cuprates [10–14]. The incommensurate lattice modulation (ILM) gives rise to diffuse scattering beyond the Bragg peaks in diffraction patterns, as generally occurs for structural ordering in small domains deviating from the order of the periodic crystallographic structure. In $Bi_2Sr_2CaCu_2O_{8+y}$ (BSCCO), the ILM produces both weak-diffuse and sharp-intense satellite diffraction peaks up to high temperatures [13–15]. The ILM is correlated with the distribution of oxygen interstitials in the SrO [16,17] and BiO layers [18]. Furthermore, ILM is also correlated with the spatial variation of the superconducting gaps [7] and Fermi surface reconstruction [19]. The inhomogeneous distribution of the ILM can thus change the spatial distribution of the

superconducting gap [20] and thus introduce a random field that breaks electronic nematic orders [21–23]. An interplay between superconducting gap fluctuations, local strain, and dopant distributions has been recently included in percolative models of high-temperature superconductivity based on which transport data have been reinterpreted [24].

Two-dimensional (2D) crystals of superconducting BSCCO is the ultimate realization of 2D superconductivity at high temperatures [25,26]. Their high electronic tunability has been demonstrated via electric-field effects [27], as well as by superconductor-to-insulator transition experiments [26,28]. Hall-effect experiments have shown the dominant role of superconducting and vortex fluctuations in the electronic transport [29]. Since the elastic properties of the atomically thin crystals can differ from those in the bulk [30], one may wonder if the properties of the ILM would also change in this extreme 2D limit.

In this work we undertake this task using scanning nano x-ray diffraction (SnXRD) imaging with spatial resolution of 70–100 nm in order to study the evolution of and the interplay between *puddlelike* domains of the two types of ILMs at the bulk and atomically thin limits, in fully superconducting BSCCO crystals. Our samples are composed of a layered perovskite near optimum doping with oxygen interstitials ($p = 0.16$ holes per Cu) subject to misfit strain [31–33], with an orthorhombic structure and incommensurate modulation along the long b axis with the period $(\lambda/b) \sim 4.7$
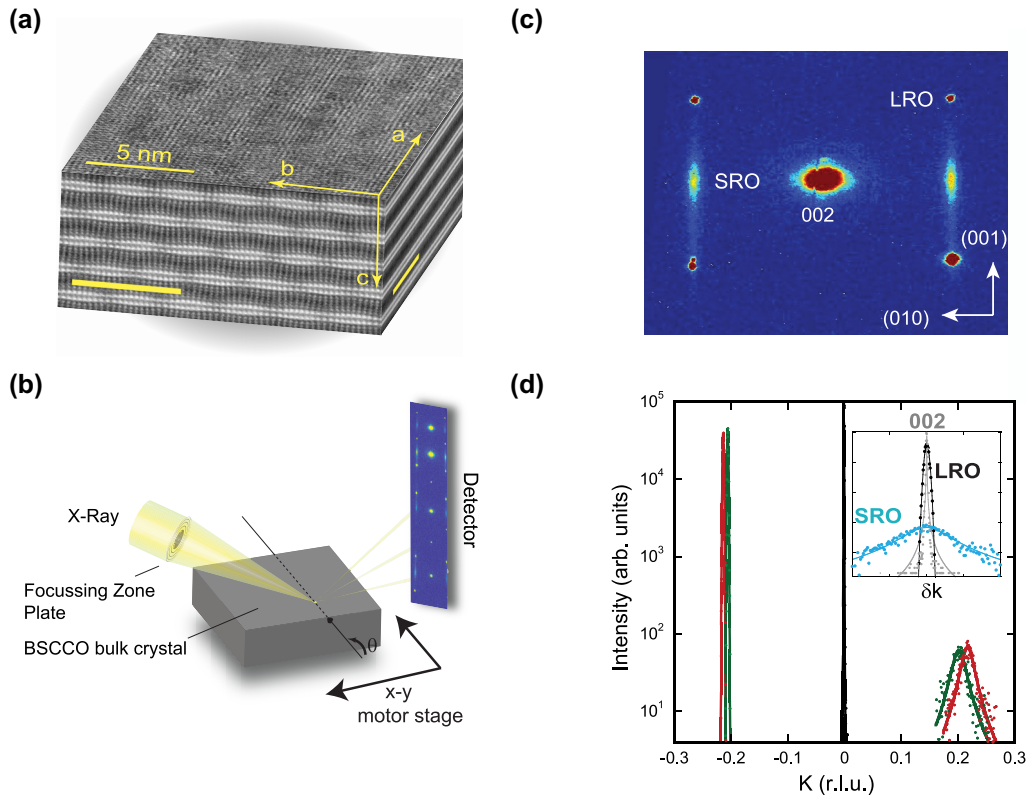

FIG. 1. Scanning nano x-ray diffraction of a BSCCO bulk single crystal. (a) Scanning transmission electron microscopy (STEM) image of the BSCCO crystal structure where the atomic structure of the incommensurate supermodulation is visible in all combinations of the $a - b - c$ crystallographic planes (see Experimental Details in [46]). (b) Schematic diagram of the SnXRD imaging setup at the Hard X-ray Nanoprobe beamline (HXN) [44,45] at the NLSL-II. An x-ray zone plate, together with a central beamstop (not shown) and an order-sorting aperture (not shown), focuses the impinging monochromatic x-ray beam with energy 12 keV down to 70 nm. The sample (a BSCCO single crystal) can be positioned in the beam by accurate translations $x - y$, while the incidence angle to sample can be controlled by θ rotation. The diffracted beam is collected by a 2D detector whose image is integrated from a wide-range angular scan. While the experiment used the horizontal diffraction geometry, we show the rotated schematic to preserve the same sample orientation as (a). (c) Reciprocal space map around the [002] Bragg peak collected during the rocking scan. The superlattice reflections due to the LRO and SRO domains of the incommensurate modulation are visible. (d) LRO (at $k = -0.21$) and SRO ($k = 0.21$) peaks, collected at two different places with tightly focused beam in the same crystal, along the best fit using a Lorentzian line shape (continuous lines). The central Bragg peaks are also shown. The cuts are taken where indicated by the labels. The insets show the profiles of the [002], LRO and SRO peaks along k direction, centered at $k = 0$, to highlight the different width peaks.

[6,8,13–15], where λ is the modulation wavelength and $b = 0.547$nm is the b-axis lattice parameter.

The ILMs are believed to originate from misfit strains between atomic layers in the BSCCO lattice of different compositions [1–9]. Such strain in the active superconducting atomic layers modifies electronic properties in parallel to the effects of doping [31] and become an important factor controlling the maximum critical temperature in the phase diagram of many families of high-temperature superconductors, ranging from cuprates [31] and diborides [32] to the iron-based superconductors [33]. This implies that in low-dimensional systems the strain fields can also control the periodic reorganization of charge on distances varying from the atomic scales [34] to mesoscales [35,36].

II. RESULTS AND DISCUSSION

Figure 1(a) shows the real-space representation of the lattice modulations in BSCCO, constructed using the

high-angle annular dark field (HAADF) scanning transmission electron microscopy (STEM) images taken along the three different crystallographic axes. The results are combined into a three-dimensional (3D) representation. The observed one-dimensional (1D) lattice modulation is running along the (010) crystal axis in real space. While these STEM images offer a convenient visualization of the crystallographic structure of 2D materials [34], the cross-sectional STEM study on atomically thin samples requires special sample preparation techniques that may change the atomic structures and cannot provide comprehensible information regarding ILMs in the 2D plane. To avoid these problems, we have visualized the spatial distribution of the ILMs using SnXRD at the bulk and atomically thin limits. In previous x-ray diffraction (XRD) studies of BSCCO [6,8,13–15], the 1D ILM has been reported to have both diffuse short-range order (SRO) satellites at $\boldsymbol{q}_s = (0, 0.21, 2n)$ and long-range order (LRO) satellites at $\boldsymbol{q}_L = (0, 0.21, 2n + 1)$ (where $\boldsymbol{q}_s$ and $\boldsymbol{q}_L$ are the reciprocal lattice units (r.l.u.) and n is an integer number) around Bragg

peaks. The LRO are 3D ILMs, while the SRO arises from the stacking-fault interfaces between the LRO domains [5,8,13].

The SnXRD measurements combined with advanced analytic tools have proven to be extremely useful for revealing the spatial correlations between the distinct lattice, charge, spin, and quenched disorder domains in cuprates [37–40], iron pnictides [41], vanadium dioxide [42], and chromium [43]. However, only a few of these experiments have properly exploited the recent technological advances in x-ray focusing, which enabled beam sizes below 100 nm [44,45]. In our experiment we reduce the beam size down to 70–100 nm in order to scan the sample in the $a − b$ direction with a scanning step of 100 nm in both directions. At each location, we obtain the XRD corresponding to the wave vector (h, k, l) in r.l.u. within the tightly focused beam spots. To study the ILMs running along the (010) crystallographic direction, we typically record the diffraction pattern in the $h = 0$ plane.

Figure 1(b) shows the schematic for the SnXRD setup. A large-scale reciprocal space map is taken by integrating the diffraction patterns over a wide range of incidence angles, measured in bulk BSCCO single crystals, while in Fig. 1(c) we zoom in on the [002] peak with the surrounding LRO and SRO superstructure peaks. We observe that the LRO and SRO peak location along (010) are modulated from spot to spot on the same sample relative to the [002] Bragg peak position. This is shown in Fig. 1(d), where we plot the XRD profiles along the (010) axis, integrated along (001) in order to simultaneously study the SRO, LRO, and the [002] Bragg peaks, for two different representative locations on the same single crystal. The scanning has been performed with the crystal at a fixed orientation where the LRO, SRO, and 002 peaks are detected, in the reciprocal space locations as indicated by the labels in Fig. 1(c). The LRO and SRO peaks change their wave vector k, while the [002] peak remains inside the experimental pixel resolution $\Delta k_{exp} = 6 \times 10^{-4}$ r.l.u. The SRO shows a broader distribution with its FWHM ~ 0.025 r.l.u., which is about ten times larger than the LRO peak (FWHM ~ 0.0025), as highlighted in the inset of Fig. 1(d). The coherence length of the ILMs can be quantitatively estimated by standard crystallographic methods using the FWHM of the satellite diffraction peaks [46]. We have found that the LRO satellite reveals a large in-plane domain size ξ_b^{LRO} above 100 nm while we have $\xi_b^{SRO} = 11$ nm for the SRO satellite, as shown in Fig. S2 and Table 1 of the Supplemental Material (SM) [46]. The broader elongation of the SRO peaks occurs also along the (001) axis, indicating the 2D nature of the SRO structures. We do observe that the in-plane domain size ξ_b is larger than the out-of-plane domain size ξ_c for both LRO and SRO modulations. In particular, we find that the out-of-plane SRO domain size ($\xi_c^{SRO} = 4.1$ nm) is slightly larger than the c axis of a single unit cell ($c = 3.1$ nm), suggesting that SRO modulations are similar to stacking faults [13] arising at the interface between different LRO domains. Furthermore, SRO peaks only appear around Bragg peaks with $l =$ even, implying that these modulations are out of phase with respect to each other.

We have used SnXRD for visualizing the spatial distribution of the LRO and SRO ILMs in real space. More precisely, we calculated and mapped the LRO and SRO wave-vector fluctuations, δk and δl, along the **k** and **l** directions,

respectively, to visualize ILM textures on the sample. The wave-vector fluctuations are defined as $\delta k = k - \langle k \rangle$ and $\delta l = l - \langle l \rangle$, where k and l are the wave vectors of the superlattice peaks along **k** and **l** directions, respectively, measured at each position, and $\langle k \rangle$ and $\langle l \rangle$ are the average values of the wave vector measured at all positions. At the same time, we use the wave-vector fluctuations δk and δl for the [002] Bragg peak to characterize and map the lattice strain. This will allow us to search for any possible links between ILM textures and the strain map in our study.

Figures 2(a) and 2(b) show maps of δk for the LRO and SRO. Figure 2(c) shows the probability density function (PDF) of the spatial in-plane LRO (red squares), SRO (black circles), and the [002] (dashed line) δk fluctuations. The gray rectangle represents the experimental resolution Δk_{exp} corresponding to a single pixel on the x-ray pixel-array detector. Both the LRO and SRO show similar PDFs, varying in the range of about $0.007 \sim 10 \Delta k_{exp}$, larger than the experimental resolution. From the spatial dependence of the SnXRD measurements, we also found that the inhomogeneities of the LRO and SRO modulations in our bulk samples are correlated to each other. This positive spatial correlation can be seen in the scatter plot of δk fluctuations of the LRO and SRO shown in Fig. 2(d), where we observe that larger LRO corresponds to larger SRO modulations. This observation indicates a close connection between the distribution of the SRO domains and inhomogeneities of the ILMs. The LRO and SRO spatial patterns do not show significant directionality in texture. Figure 2(e) shows the directional distribution of $\nabla \delta k$ for the LRO and SRO, computed from the δk maps. Here we can see that the spatial variations of δk are isotropic for both LRO and SRO.

In the out-of-plane **l** direction, we find that the δl fluctuations of LRO and [002] remain quite homogeneous within the experimental resolution, $\Delta l_{exp} = 0.005$ r.l.u., while the map of the δl fluctuations of SRO shows larger fluctuations (see Fig. S3, SM [46]). Hence the positive correlation between the LRO and SRO inhomogeneities is a 2D structural feature occurring in the $a − b$ plane of the bulk sample. In the bulk sample both δk and δl fluctuations of the [002] Bragg peak remain below the experimental resolution.

Now we move to exploit the spatial imaging capability of the SnXRD to investigate the spatial distribution of lattice modulations in atomically thin BSCCO crystals [see Fig. 3(a)]. In this experiment we employ a two-unit-cell (u.c.) thick (6 nm thick in atomic force microscope measurements) BSCCO sample about 50 um in lateral size, obtained by mechanical exfoliation. This crystal was subsequently encapsulated and protected by atomically thin hexagonal boron nitride (hBN) crystals (see Methods and Fig. S1, SM [46]). For atomically thin BSCCO crystals, protecting the crystals with chemically inert hBN is necessary to form a van der Waals (vdW) protective layer that prevents degradation of the samples. After creating the hBN/BSCCO heterostructure on the SiO_2/Si substrate, we also deposit gold markers [see Fig. 3(b)] necessary for alignment with the hard x-ray nanobeam's region of interest (see Methods [46]). Figure 3(c) shows the reciprocal space map around the [002] peak collected during the rocking scan. Despite the 2-u.c. thickness of the atomically thin crystals, both the SRO and the LRO satellites are detectable [see Fig. 3(c)], although their intensity results are reduced in comparison with the bulk sample. This
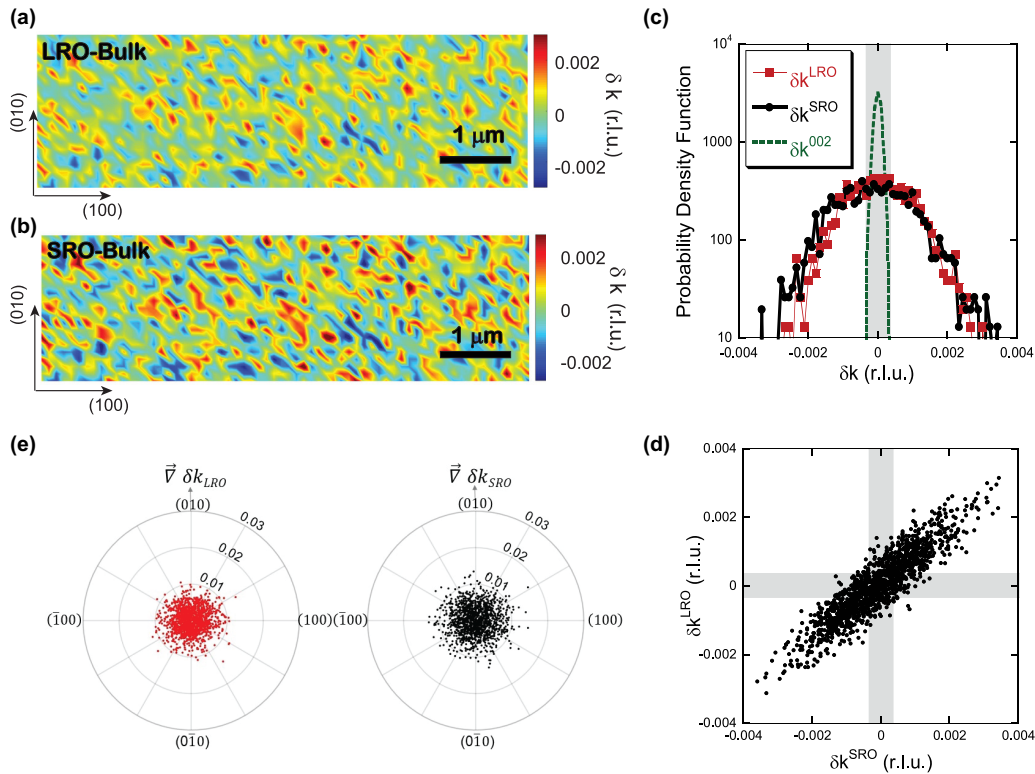
FIG. 2. Spatial complexity of the incommensurate lattice modulations in the BSCCO bulk crystal illustrated by scanning nano x-ray diffraction maps showing the spatial variation of the propagation vector δk of (a) LRO and (b) SRO peaks. The red (blue) spots correspond to sample regions with higher (lower) wave vectors with respect to the average of 0.21 r.l.u. (c) Probability density function of δk calculated from the (red full squares) LRO and (black full circles) SRO maps. We report also the variation for the [002] Bragg peak position along the k direction, which remains inside the experimental resolution indicated by shadowed rectangle corresponding to $\Delta k_{\mathrm{exp}} = 0.0006$ r.l.u for a single pixel. (d) Scatter plot of LRO peak propagation vector deviations vs SRO peak demonstrating the positive spatial correlation between LRO and SRO modulations. The gray rectangles correspond to the experimental resolution Δk_{exp}. (e) Polar plots of the gradient magnitude vs gradient direction of (left panel) LRO and (right panel) SRO $\nabla \delta k$ calculated from the maps in panels (a) and (b).

observation is in sharp contrast to the previous XRD experiments performed on the unprotected BSCCO flakes where no SRO peaks were detected [47], suggesting that indeed the hBN encapsulation is necessary for protecting the chemical integrity of the atomically thin BSCCO samples.

Figure 3(d) shows the line shape of the LRO and SRO profiles along the (010) direction. The XRD profiles measured at different sample spots show significant differences in width, position, and amplitude. We find that the LRO domain size, $\xi_{\mathrm{b}}^{\mathrm{LRO}}$, decreases in atomically thin crystals. At the 2D limit, $\xi_{\mathrm{b}}^{\mathrm{LRO}}$ becomes equal to 15 nm, which is an order of magnitude smaller than the value of $\sim$100 nm obtained in the bulk sample (see Table 1, SM [46]). It is interesting to note that the domain size for the SRO decreases only slightly from 11 nm in the bulk to 7 nm in the 2-u.c. atomically thin crystals (see Fig. S2 and Table 1, SM [46]). As the thickness of the sample is only 6 nm, the c-axis structural coherence lengths are strongly reduced along the (001) direction: ξ_{c} becomes about 1 and 2.5 nm for the SRO and LRO modulations, respectively, as compared to 4 and 94 nm in the bulk sample.

Spatial XRD imaging of the SRO/LRO in the 2-u.c. sample reveals the effect of the reduced dimensionality to the ILMs. Figures 4(a) and 4(b) show spatial maps of δk for LRO and SRO wave vectors, where a different texture appears in

comparison with those of the bulk sample. In order to quantify these textures, we have calculated the probability density function, the spatial correlations, and the gradient of the maps of δk and δl fluctuations. Although fluctuations for the LRO and SRO show a similar range to what is found in the bulk [Fig. 2(c)], the corresponding probability density function deviates strongly from the Gaussian-like distribution characteristic of the bulk. The spatial correlations between the LRO and SRO, shown in Fig. 4(d), become anticorrelated, in sharp contrast to observed correlations in the bulk crystal. We also observe directional textures of the fluctuation pattern in the 2-u.c. flake that is absent in the bulk crystal. Unlike the bulk sample [Fig. 2(e)], Fig. 4(e) shows that the angular-dependent $\nabla \delta k$ displays a preferred direction near -90°, corresponding to the (0-10) direction, where the δk fluctuations are larger. The negative spatial correlations between the LRO and SRO and the directional textures have also been found along the (001) direction (see Fig. S4, SM [46]). The different correlations between the SRO and LRO, from the bulk to the atomically thin crystals, are even more evident by visualizing in-plane δk, as a function of out-plane, δl fluctuations (see Fig. S5, SM [46]), suggesting a different correlated disorder [48] with an emerging spatial pattern appears in atomically thin BSCCO samples.
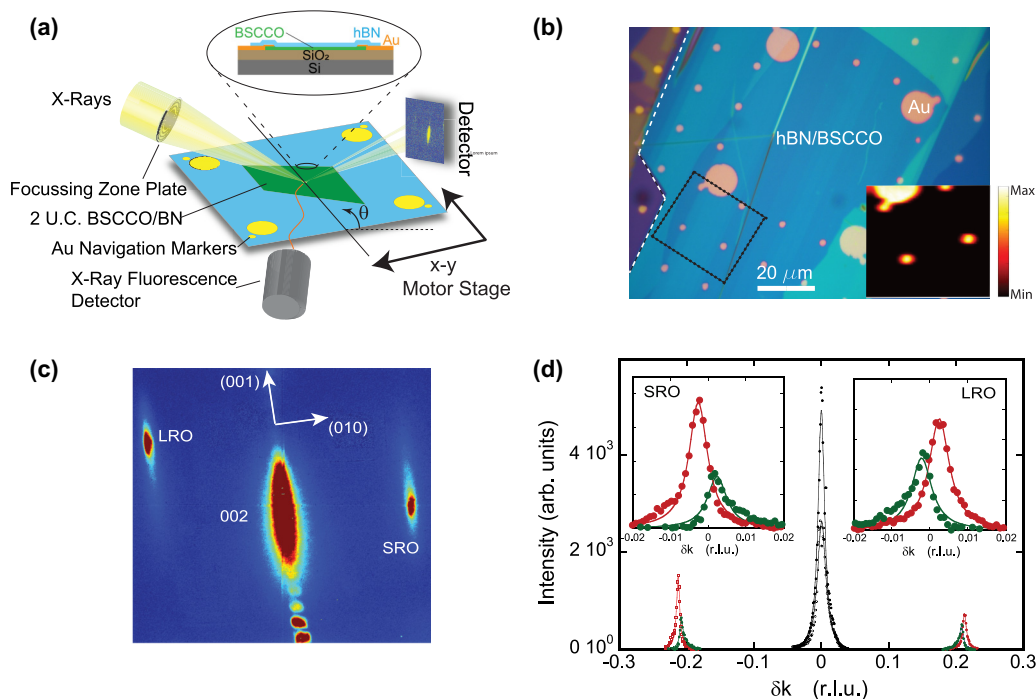
FIG. 3. Scanning nano x-ray diffraction of a BSCCO VdW heterostructure. (a) The x-ray beam is focused on an atomically thin VdW BSCCO heterostructure. We used a similar experimental setup of Fig. 1(b), adding an x-ray fluorescence detector to locate the sample using gold markers deposited on the top of the VdW heterostructure. The x-ray detector records the diffraction pattern in the illuminated sample area from a cuprate crystal 6 nm thick (2 u.c.). (b) Optical image showing the gold marker array deposited on top of the VdW heterostructure. Inset shows a typical fluorescence map of the area in dashed box. (c) A portion of $b^* - c^*$ diffraction pattern where the [002] peak and the superlattice reflections for LRO and SRO incommensurate modulation are indicated. (d) Two typical LRO and SRO peaks along the k direction, collected at two different places on the same heterostructure. The insets highlight the δk fluctuations for both LRO and SRO modulations.

A possible explanation for the origin of these differences can be that the misfit strain between the Bi-O rocksalt and the Cu-Sr-Ca perovskite layers [31–33] could change at a reduced dimensionality. Indeed, we find that the variation of the [002] peak is slightly larger than the experimental resolution Δk_{exp}, as shown in Fig. 4(c). This result indicates that the intrinsic strain of an atomically thin crystal plays a role in the different spatial arrangements of the incommensurate lattice modulations. The fluctuations of the [002] peak exceed the experimental resolution Δk_{exp} just for the 2-u.c. thin sample. This behavior is accentuated along the (001) direction, where the [002] peak is clearly larger than Δl_{exp} (see Fig. S4, SM [46]). This unusual distribution might indicate some structural instability and the related criticality [37–39] in the flake and calls for a further thorough investigation.

III. CONCLUSION

In summary, highly resolved scanning synchrotron x-ray diffraction measurements around the [002] Bragg peak on both a bulk sample and an atomically thin BSCCO van der Waals heterostructure has enabled us to collect simultaneously (i) SRO, (ii) LRO, and (iii) [002] Bragg peaks. We have visualized the spatial distributions of the LRO and SRO wave vectors by displaying variations of δk and δl, along the **k** and **l** direction, respectively. At the same time, we have found variations of the wave vector of the [002] Bragg

peak to characterize and visualize the lattice strain maps. Our results shown in Fig. 2(c) and Fig. S3, SM [46] reveal that the bulk sample does not experience a significant strain since the variation δk and δl of the (002) peak are both below the experimental resolution. In this case, the LRO and SRO textures comprise randomly arranged puddles at the nanoscale, as shown in the maps in Figs. 2(a) and 2(b), respectively, with no preferential direction. On the contrary, the appreciable lattice strain in the 2-u.c. sample is seen when both δk and δl become larger than the experimental resolution. In this case, the LRO and SRO modulations form spatial patterns. The larger strains indicate more intense electron-lattice interactions; therefore one can expect that in this case, the lattice modulations are accompanied by the corresponding charge-density modulations (or charge-density waves), which arise to maintain neutrality. Then the spatial charge modulations should form the charge modulation puddles on comparable mesoscales. These are mapped in Figs. 4(a) and 4(b). The influence of the mesoscale strains on the mesoscale texture can be depicted by inspecting spatial correlations between the textures of the LRO and the (002) Bragg peak along both δk and δl directions in Fig. S6, SM [46]. In the 2-u.c. sample we observe positive correlations between δk of (002) and LRO peaks and somewhat larger negative correlations between δl of (002) and LRO modulation peaks. This is expected for multilayered structures where larger fluctuations occur in the out-of-plane direction. In our case, since the
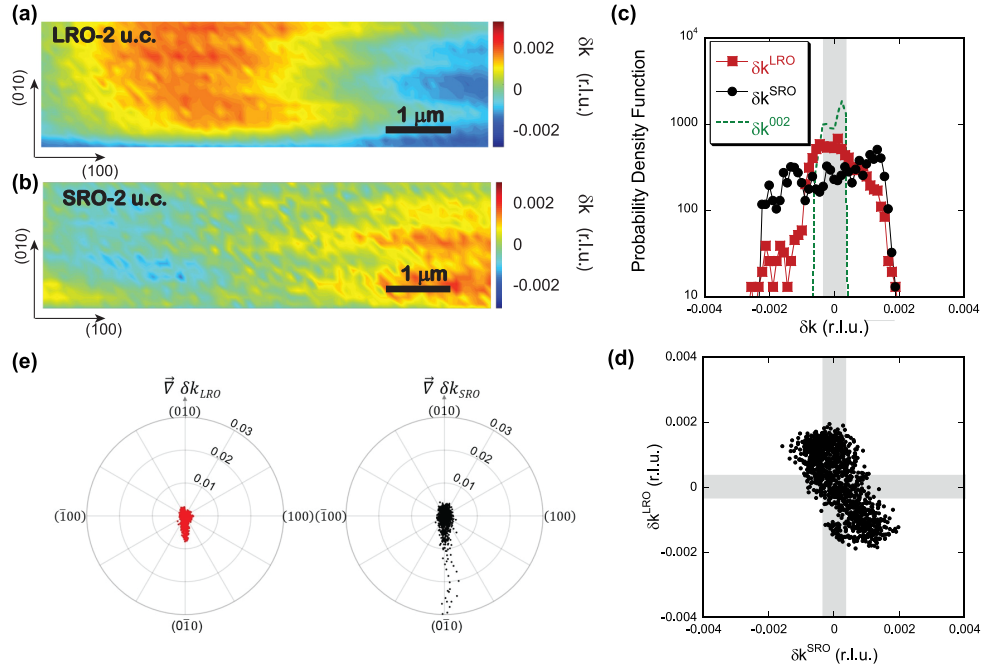
FIG. 4. Spatial complexity of the incommensurate lattice modulations in the VdW heterostructure. Scanning nano x-ray diffraction map of a region of interest showing the spatial variation along the (010) direction, δk, of the LRO peak (panel a) and the SRO peak (panel b). The red (blue) spots correspond to sample regions with a higher (lower) propagation wave vector with respect to the average value of 0.21 (green color). (c) Probability density function of δk calculated from the LRO (red squares), the SRO (black circles), and the [002] peak (dashed green line) maps. In this case, the variation of the [002] peak exceeds the experimental resolution, Δk_{exp}, indicated by the shadowed area. (d) Scatter plot of δk for the (black circles) LRO vs SRO showing an anticorrelation between LRO and SRO. The shadowed rectangles correspond to the experimental resolution. (e) Polar plots of the gradient magnitude vs gradient direction of (left panel) LRO and (right panel) SRO calculated from the δk maps shown in panels (a) and (b). In this case we observe preferential directions of the grain arrangement in the δk maps along the (0-10) direction.

δk fluctuations of the LRO are anticorrelated with δk of the SRO [Fig. 2(d)], there exists a weak positive correlation between the in-plane strain and the SRO modulation, see Fig. S6a, SM [46].

The observed modulations, which appear to be in concert with the findings of Yu *et al.* [26], stem from the misfit strain arising from the mismatch between the substrate and thin BSCCO flakes. These inhomogeneous ILMs may have a profound effect on the electronic properties of heterostructures. In particular, one may develop a theoretical framework to describe the interaction between transport carrier and inhomogeneous ILMs using a similar theoretical technique adopted for the inhomogeneous charge-density waves interacting with the carriers [49]. Potentially, this approach can explain the striking observation that the electronic mobility in the atomically thin films is reduced, while the Hall resistance remains intact and does not change much as compared to the bulk value [28]. Finally, our findings indicate that a fine-tuning of the strain can be used to control the spatial correlations of the ILMs, providing a route for investigating and controlling correlated disorder [5] and its relation to electronic functionality in 2D high-temperature superconductors.

[1] V. Kresin, Y. Ovchinnikov, and S. Wolf, Phys. Rep. **431**, 231 (2006).

[2] J.-H. She and J. Zaanen, Phys. Rev. B **80**, 184518 (2009).

[3] W. B. Gao, Q. Q. Liu, L. X. Yang, Y. Yu, F. Y. Li, C. Q. Jin, and S. Uchida, Phys. Rev. B **80**, 094523 (2009).

[4] T. H. Geballe, R. H. Hammond, and P. M. Wu, Physica C (Amsterdam, Neth.) **514**, 9 (2015).

[5] A. Bianconi, A. Valletta, A. Perali, and N. L. Saini, Physica C **296**, 269 (1998).

[6] A. Yamamoto, M. Onoda, E. Takayama-Muromachi, F. Izumi, T. Ishigaki, and H. Asano, Phys. Rev. B **42**, 4228 (1990).

[7] J. A. Slezak, J. Lee, M. Wang, K. McElroy, K. Fujita, B. M. Andersen, P. J. Hirschfeld, H. Eisaki, S. Uchida, and J. C. Davis, Proc. Natl. Acad. Sci. **105**, 3203 (2008).

[8] A. Bianconi, M. Lusignoli, N. L. Saini, P. Bordet, A. Kvick, and P. G. Radaelli, Phys. Rev. B **54**, 4310 (1996).

[9] J. Zaanen, Nature (London) **466**, 825 (2010).

[10] P. G. Radaelli, J. D. Jorgensen, A. J. Schultz, B. A. Hunter, J. L. Wagner, F. C. Chou, and D. C. Johnston, Phys. Rev. B **48**, 499 (1993).

[11] Y. Koyama, S.-I. Nakamura, Y. Inoue, and T. Ohno, Phys. Rev. B **46**, 5757 (1992).

[12] W. Dmowski, R. J. McQueeney, T. Egami, Y. P. Feng, S. K. Sinha, T. Hinatsu, and S. Uchida, Phys. Rev. B **52**, 6829 (1995).

[13] J. P. Castellan, B. D. Gaulin, H. A. Dabkowska, A. Nabialek, G. Gu, X. Liu, and Z. Islam, Phys. Rev. B **73**, 174505 (2006).

[14] M. Izquierdo, S. Megtert, J. P. Albouy, J. Avila, M. A. Valbuena, G. Gu, J. S. Abell, G. Yang, M. C. Asensio, and R. Comes, Phys. Rev. B **74**, 054512 (2006).

[15] R. Comes, M. Izquierdo, S. Megtert, P. A. Albouy, J. Avila, M. A. Valbuena, G. Gu, J. S. Abell, and M. C. Asensio, Physica C **460**, 730 (2007).

[16] I. Zeljkovic, J. Nieminen, D. Huang, T. R. Chang, Y. He, H. T. Jeng, Z. Xu, J. Wen, G. Gu, H. Lin, and R. S. Markiewicz, Nano Lett. **14**, 6749 (2014).

[17] I. Zeljkovic, Z. Xu, J. Wen, G. Gu, R. S. Markiewicz, and J. E. H, Science **337**, 320 (2012).

[18] I. Zeljkovic, E. J. Main, T. L. Williams, M. C. Boyer, K. Chatterjee, W. D. Wise, Y. Yin, M. Zech, A. Pivonka, T. Kondo, T. Takeuchi et al., Nat. Mater. **11**, 585 (2012).

[19] T. Valla, I. Pletikosic, I. K. Drozdov, and G. D. Gu, Phys. Rev. B **100**, 241112(R) (2019).

[20] C. H. Howald, H. Eisaki, N. Kaneko, and A. Kapitulnik, Proc. Natl. Acad. Sci. USA **100**, 9705 (2003).

[21] E. W. Carlson and K. A. Dahmen, Nat. Commun. **2**, 379 (2011).

[22] E. W. Carlson, L. Shuo, B. Phillabaum, and K. A. Dahmen, J. Supercond. Novel Magn. **28**, 1237 (2015).

[23] F. Y. Massee, K. Huang, M. S. Golden, and M. Aprili, Nat. Commun. **10**, 544 (2019).

[24] D. Pelc, M. Vučković, M. S. Grbić, M. Požek, G. Yu, T. Sasagawa, M. Greven, and N. Barišić, Nat. Commun. **9**, 4327 (2018).

[25] Y. Saito, T. Nojima, and Y. Iwasa, Nat. Rev. Mater. **2**, 16094 (2017).

[26] Y. Yu, L. Ma, P. Cai, R. Zhong, C. Ye, J. Shen, G. D. Gu, X. H. Chen, and Y. Zhang, Nature (London) **575**, 156 (2019).

[27] E. Sterpetti, J. Biscaras, A. Erb, and A. Shukla, Nat. Commun. **8**, 2060 (2017).

[28] M. Liao, Y. Zhu, J. Zhang, R. Zhong, J. Schneeloch, G. Gu, K. Jiang, D. Zhang, X. Ma, and Q.-K. Xue, Nano Lett. **18**, 5660 (2018).

[29] S. Y. Frank Zhao, N. Poccia, M. G. Panetta, C. Yu, J. W. Johnson, H. Yoo, R. Zhong, G. D. Gu, K. Watanabe, T. Taniguchi, S. V. Postolova, V. M. Vinokur, and P. Kim, Phys. Rev. Lett. **122**, 247001 (2019).

[30] S. K. Kumar, D. Jangade, A. Thamizhavel, M. M. Deshmukh, and V. Singh, Appl. Phys. Lett. **115**, 143102 (2019).

[31] S. Agrestini, N. L. Saini, G. Bianconi, and A. Bianconi, J. Phys. A Math. Gen. **36**, 9133 (2003).

[32] S. Agrestini, C. Metallo, M. Filippi, L. Simonelli, G. Campi, C. Sanipoli, E. Liarokapis, S. De Negri, M. Giovannini, A. Saccone, A. Latini, and A. Bianconi, Phys. Rev. B, **70**, 134514 (2004).

[33] A. Ricci, N. Poccia, B. Joseph, L. Barba, G. Arrighetti, G. Ciasca, J.-Q. Yan, R. W. McCallum, T. A. Lograsso, and N. D. Zhigadlo, Phys. Rev. B **82**, 144507 (2010).

[34] S. Gao, F. Flicker, R. Sankar, H. Zhao, Z. Ren, B. Rachmilowitz, S. Balachandar, F. Chou, K. S. Burch, Z. Wang et al., Proc. Natl. Acad. Sci. USA **115**, 6986 (2018).

[35] A. F. Isakovic, P. G. Evans, J. Kmetko, K. Cicak, Z. Cai, B. Lai, and R. E. Thorne, Phys. Rev. Lett. **96**, 046401 (2006).

[36] H. Yoo, R. Engelke, S. Carr, S. Fang, K. Zhang, P. Cazeaux, S. H. Sung, R. Hovden, A. W. Tsen, T. Taniguchi et al., Nat. Mater. **18**, 448 (2019).

[37] M. Fratini, N. Poccia, A. Ricci, G. Campi, M. Burghammer, G. Aeppli, and A. Bianconi, Nature (London) **466**, 841 (2010).

[38] N. Poccia, A. Ricci, G. Campi, M. Fratini, A. Puri, D. Di Gioacchino, A. Marcelli, M. Reynolds, M. Burghammer, N. L. Saini et al., Proc. Natl. Acad. Sci. USA **109**, 15685 (2012).

[39] G. Campi, A. Bianconi, N. Poccia, G. Bianconi, L. Barba, G. Arrighetti, D. Innocenti, J. Karpinski, N. D. Zhigadlo, S. M. Kazakov et al., Nature (London) **525**, 359 (2015).

[40] J. Zhang, Y. Ding, C.-C. Chen, Z. Cai, J. Chang, B. Chen, X. Hong, A. Fluerasu, Y. Zhang, C.-S. Ku et al., J. Phys. Chem. Lett. **9**, 4182 (2018).

[41] A. Ricci, N. Poccia, B. Joseph, D. Innocenti, G. Campi, A. Zozulya, F. Westermeier, A. Schavkan, F. Coneri, A. Bianconi et al., Phys. Rev. B **91**, 020503(R) (2015).

[42] A. Singer, J. G. Ramirez, I. Valmianski, D. Cela, N. Hua, R. Kukreja, J. Wingert, O. Kovalchuk, J. M. Glownia, M. Sikorski et al., Phys. Rev. Lett. **120**, 207601 (2018).

[43] P. G. Evans, E. D. Isaacs, G. Aeppli, Z. Cai, and B. Lai, Science **295**, 1042n (2002).

[44] H. Yan, N. Bouet, J. Zhou, X. Huang, E. Nazaretski, W. Xu, A. P. Cocco, W. K. S. Chiu, K. S. Brinkman, and Y. S. Chu, Nano Futures **2**, 011001 (2018).

[45] E. Nazaretski, H. Yan, K. Lauer, N. Bouet, X. Huang, W. Xu, J. Zhou, D. Shu, Y. Hwu, and Y. S. Chu, J. Synchrotron Radiat. **24**, 1113 (2017).

[46] See Supplemental Material at http://link.aps.org/supplemental/10.1103/PhysRevMaterials.4.114007 for methods and detailed analysis.

[47] A. Lupascu, R. Feng, L. J. Sandilands, Z. Nie, V. Baydina, G. Gu, S. Ono, Y. Ando, D. C. Kwok, N. Lee et al., Appl. Phys. Lett. **101**, 223106 (2012).

[48] A. Augieri, F. Rizzo, V. Galluzzi, A. Mancini, F. Fabbri, A. A.Armenio, A. Vannozzi, V. Pinto, A. Rufoloni, L. Piperno et al., IEEE Trans. Appl. Supercond. **28**, 7500604 (2018).

[49] A. A. Sinchenko, R. V. Chernikov, A. A. Ivanov, P. Monceau, T. Crozes, and S. A. Brazovskii, J. Phys.: Condens. Matter **21**, 435601 (2009).